Journal of Materials Chemistry C

PAPER

View Article Online
View Journal

Cite this: DOI: 10.1039/c9tc05490a

High-sensitivity X-ray detectors based on solution-grown caesium lead bromide single crystals†

Hongjian Zhang,[ab] Fangbao Wang,[a] Yufei Lu,[b] Qihao Sun,[a] Yadong Xu,*[a] Bin-Bin Zhang,*[a] Wanqi Jie[a] and Mercouri G. Kanatzidis[c]

Received 8th October 2019,
Accepted 6th November 2019

DOI: 10.1039/c9tc05490a

rsc.li/materials-c

X-ray detection is of great significance for medical diagnostics, industrial non-destructive inspection, nuclear plants and scientific research. However, high sensitivity is needed for X-ray detectors to reduce the radiation dose applied to human bodies for the applications of medical imaging and security checks. Here, we reported sensitive X-ray detectors made of solution-grown inorganic lead perovskite $CsPbBr_3$ single crystals and the synthesis of high-quality inorganic lead perovskite $CsPbBr_3$ single crystals using an improved low temperature solution method, which exhibited high transmittance, mobility and mobility–lifetime products. By designing the detector in an asymmetric electrode configuration, ion migration was effectively suppressed under a high voltage with a low dark current and an outstanding photoresponse. The optimized detector exhibited high sensitivity of 1256 μC Gy^{-1} cm^{-2} for 80 kVp X-ray detection under a relatively low electric field of 20 V mm^{-1}, which was 60 times higher than that of commercially used α-Se detectors. Due to its facile synthesis, low cost, long-term stability, and high detection sensitivity, $CsPbBr_3$ is expected to be an outstanding candidate for commercialized sensitive X-ray detectors.

1. Introduction

X-ray detection is of utmost importance for wide applications in the fields of medical diagnostics, industrial non-destructive inspection, nuclear power plants and scientific research.[1–3] In all the X-ray detection semiconductors, high sensitivity and detection efficiency are paramount properties to reduce the X-ray dose that patients and workers are exposed to during X-ray inspections such as computed tomography.[4–6] Thus, enhancing the sensitivity of X-ray detectors has important significance to reduce the risks of cancer and simultaneously obtain high-resolution images. For semiconductor-based X-ray detectors, the current state-of-the-art materials used as X-ray detectors include amorphous Se (α-Se),[7] PbI_2,[8] HgI_2,[9,10] CdTe[11] and CdZnTe.[12] The application of commercialized α-Se is limited because of its low absorption ability for higher energy X-rays over 50 keV. For PbI_2 and HgI_2, stability issues hinder their further applications in X-ray detection. CdTe and CdZnTe seem to have promising prospects; however, their high cost and complicated technology processes must be taken into consideration for their wide applications.[13]

Recently, metal halide perovskites with the general formula of ABX_3 (A = CH_3CH_3, $NH_2CH{=}NH_2$, and Cs; B = Pb, Bi, and Sn; and X = I, Br, and Cl) have been widely studied because of their remarkable performances in solar cells,[14–16] lasing,[17,18] and LEDs[17,19] and their facile synthesis methods. Due to their high-Z elements such as Cs, Pb, Bi, I and Br and high mobility–lifetime ($\mu\tau$) products, these perovskites are considered as potential materials for a new generation of nuclear radiation detectors. To date, $MAPbI_3$ thin films,[20] $MAPbI_3$ sintered wafers,[21] $MAPbBr_3$ single crystals (SCs),[22,23] and $Cs_2AgBiBr_6$ SCs[24] have been demonstrated to be successfully applied in X-ray detection. However, their issues such as high density of defects in their crystals, low sensitivity, ion migration under high electric field, and poor stability are still severe enough to hinder their further applications.

Accordingly, several efforts have been made to try to tackle these problems. For example, thermal annealing and surface treatment have been proven to be effective measures to improve the surface state of the crystals and carrier transportation.[24,25] In addition, special device designs that use asymmetric electrodes[26,27] or employ metal oxides such as aluminum zinc oxide as electrodes[25] have also been demonstrated to significantly decrease the leakage current of the device by increasing the Schottky barrier or forming p–n junction structures. As a stable perovskite material without organic molecules,[28–32] cesium lead bromide ($CsPbBr_3$) has received much attention.

[a] State Key Laboratory of Solidification Processing, Key Laboratory of Radiation Detection Materials and Devices, & School of Materials Science and Engineering, Northwestern Polytechnical University, Xi'an 710072, China. E-mail: xyd220@nwpu.edu.cn, zbb@nwpu.edu.cn
[b] Institute of Flexible Electronics (IFE), Northwestern Polytechnical University (NPU), Xi'an 710072, China
[c] Department of Chemistry, Northwestern University, Evanston, IL 60208, USA

† Electronic supplementary information (ESI) available. See DOI: 10.1039/c9tc05490a

$CsPbBr_3$ possesses an effective atomic number, Z_{eff}, of 65.9, with high attenuation coefficient for absorbing X-rays. $CsPbBr_3$ microcrystals[33] and quasi-monocrystalline[34] thick films have been reported recently as X-ray detectors, but controlling the film quality was challenging and the density of defects in the film was high. The optoelectronic properties related to lifetimes, carrier mobilities and defect tolerance of single crystals show better performances than those of polycrystalline materials.[35,36] However, the fabrication of X-ray detectors using $CsPbBr_3$ SCs has not been reported so far.

In this work, we demonstrate the application of solution-grown $CsPbBr_3$ SCs to fabricate X-ray detectors with high sensitivity. $CsPbBr_3$ SCs were grown *via* an improved inverse temperature crystallization (ITC) method with high crystallization quality. By designing the device configuration into asymmetric electrodes, the device degradation caused by ion migration was effectively prevented under relatively high bias voltages. Additionally, X-ray detectors with high sensitivities were fabricated using the improved device structure.

2. Materials and methods

2.1. Materials

CsBr ($\geq$99.5%), $PbBr_2$ ($\geq$99.5%), dimethyl sulfoxide (DMSO, $\geq$99.8%), dimethylformamide (DMF, $>$99.8%) and cyclohexanol (CyOH, $\geq$99.8%) were purchased from Sigma-Aldrich.

2.2. Growth of $CsPbBr_3$ single crystals and device fabrication

$PbBr_2$ (1 M) and CsBr (0.5 M) were dissolved in 60 mL DMSO solution and fully stirred to obtain a 2 molar ratio of $PbBr_2$ to CsBr. Then 60 mL of a mixture of CyOH/DMF was added to the DMSO solution to obtain the precursor solution. To achieve uniform heating, a $1 \times 1 \times 1$ m^3 water bath tank was adopted as the heating system. The water bath tank was equipped with a thermometer, thermocouple, and submersible pump. During the heating process, precise temperature compensation could be accurately controlled based on the proportion, integral, derivative (PID) adjustment. The precursor solution was put into the heating bath and maintained at the temperature of 50 °C for 12 h. After heating at a constant temperature, the solution was filtered into a new container using 30 μm sized filter paper to remove impurities and small $CsPbBr_3$ crystals. After oversaturation at 50 °C, the was heated solution at a heating rate of 1 °C per day starting from 49.5 °C. After about 10 days growth, several square-shaped $CsPbBr_3$ crystals with a size of 4–5 mm were formed on the bottom of the container. The as-grown crystals acted as seed crystals and continued to grow into large-sized $CsPbBr_3$ SCs. Detector I was prepared with a $3 \times 4 \times 1$ mm^3 $CsPbBr_3$ SC with gold electrodes evaporated on both sides. Detector II was prepared with a $5 \times 5 \times 2$ mm^3 $CsPbBr_3$ SC with aluminium and gold evaporated on each side separately. The area of each metal electrode was 3.14 mm^2.

2.3. Characterization measurements

X-ray diffraction (XRD) patterns of both the powder and single crystal samples were collected using a D/Max2500PC with $CuK_{\alpha 1}$ in the 2θ range of 10–70°. UV-Vis spectra of the $CsPbBr_3$ crystals were measured on a UV-2550 spectrometer with an integrating sphere over the spectral range of 300–1500 nm. TRIAX 550 fluorescence spectroscopy was used to collect photoluminescence (PL) time-resolved photoluminescence (TRPL) spectra, with the excitation wavelength of 325 nm. Current–voltage (*I–V*) was measured using an electrical properties measurement system (Agilent 4155C).

2.4. Radiation detection measurements

For α-particle-induced pulse shape rise time analysis, the device was exposed to the illumination of an uncollimated ^{241}Am @ 5.49 MeV α-particle source. The pulse shape information was simultaneously recorded by connecting the pre-amplifier (Model ORTEC570) and output to a high-speed waveform digitizer card. For X-ray detection measurements, a tungsten target X-ray tube (SPELLMAN XRB011) was used as the source. The X-ray source was constantly operated with the tube voltage from 40 kV to 80 kV, and the tube current was tuned from 0 to 600 μA. The X-ray dose rate was directly proportional to the tube current, and it was carefully calibrated using a thermoluminescence meter. The $CsPbBr_3$ device was placed in a dark shielding box to prevent disturbance from ambient light. The bias voltage was applied on the device and the induced photocurrent was recorded by a Keithley 6517B.

3. Results and discussion

3.1. Crystal growth and characterization

High-quality single crystals are needed for the fabrication of high-sensitivity X-ray detectors. Among the solution growth methods, the AVC method has been prevalent because of its simplicity. However, the repeatability and growth speed control of this method are not satisfactory. Thus, we employed the ITC method to grow $CsPbBr_3$ single crystals, and their growing speed could be accurately controlled by adjusting the heating rate. In our previous work,[37] we systematically studied the AVC method and found that the mole ratio of $PbBr_2$ and CsBr (n:1) is the key factor to obtain a single $CsPbBr_3$ phase and high-quality crystals. Likewise, to make crystals grow in a Br-rich solution and ensure no other phases precipitate, we set the initial mole ratio of 2:1 in the precursor. Previous research[31] showed that for the ratio of 2:1, the solubility of $CsPbBr_3$ declines significantly in the range of 75–90 °C. The range of temperature for the solubility drop can be widened to 25–110 °C with the addition of a CyOH/DMF mixture to the precursor solution. By using a water bath heating system (ESI,† Fig. S1), $CsPbBr_3$ precipitated in a specific temperature range with its solubility decreased. The heating rate should be as low as possible to ensure good crystallization quality. Fig. 1a shows the single crystals grown by the ITC method in the temperature range of 50–60 °C at the heating rate of 1 °C per day. $CsPbBr_3$ suffers from two phase transitions, which occur at around 130 °C from cubic ($Pm\bar{3}m$) to tetragonal ($P4/mbm$) and 88 °C from tetragonal ($P4/mbm$) to orthorhombic ($Pbnm$) phase.[28]

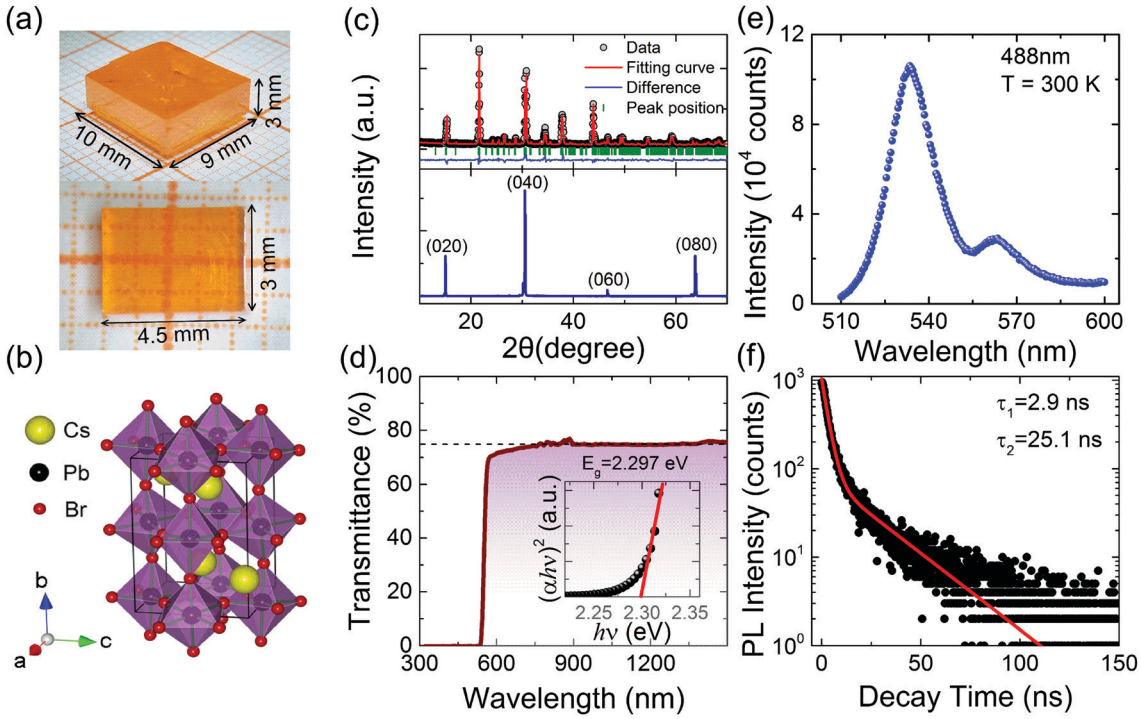

Fig. 1 (a) As-grown $CsPbBr_3$ crystals with orange color grown by the ITC method in the temperature range of 50–60 °C. (b) Schematic of the crystal structure with the space group *Pnma*. (c) XRD patterns of the powder and single-crystal samples. (d) Optical transmittance spectra for as-grown $CsPbBr_3$ crystals. The insert shows the energy gap is fitted as 2.297 eV by the Tauc plot. (e) Photoluminescence (PL) spectra of $CsPbBr_3$ crystals at 300 K. (f) PL lifetime decay upon two-photon excitation. The dots represent experimental data and the solid curve is the best fit with a double-exponential function.

However, in this growth process (50–60 °C), phase transitions were successfully avoided, which reduced the defects originating from crystal lattice transformations. Millimeter-sized, high-transparent $CsPbBr_3$ single crystals were obtained within 10 days. The centimeter-sized single crystals were grown with seed crystals.

A schematic of the $CsPbBr_3$ crystal structure at room temperature is shown in Fig. 1b, which shows the perovskite crystal structure known as ABX_3. Fig. 1c shows the powder and single crystal XRD patterns. The results of the XRD pattern refinement demonstrate that the resulting $CsPbBr_3$ has the space group of *Pnma*, with cell parameters a = 8.37 Å, b = 12.011 Å, c = 8.425 Å, $\alpha = \beta = \gamma = 90°$. It is notable that no other phase precipitated during the growth process. The single crystal pattern shows that the as-grown $CsPbBr_3$ single crystals exhibit a set of (0 l 0) diffraction surfaces. The optical properties of $CsPbBr_3$ grown *via* the ITC method were studied at room temperature. Fig. 1d shows the UV-Vis transmission spectrum from 300 nm to 1500 nm of $CsPbBr_3$. A sharp rise at around 550 nm is observed, which demonstrates the low density of the shallow energy level defects and high purity of the crystal. From 550 nm to 1500 nm, a relatively high transmittance of ~75% was obtained, which is higher than that of the crystals (~57%) grown *via* the improved AVC method[37] in our previous work, which indicates higher crystalline quality. The inset in Fig. 1d shows the Tauc plot fitting, and the band gap of the as-grown $CsPbBr_3$ was fitted as ~2.297 eV, which is in agreement with the previous crystals grown by solution methods and melting methods.[37,38] The band gap value shows that $CsPbBr_3$ is suitable for application as a photodetector.[28,31] The $CsPbBr_3$ single crystal exhibited strong PL at room temperature with 325 nm excitation. Two PL peaks located at around 530 nm and 560 nm with strong intensities were observed in the PL spectrum, as is shown in Fig. 1e, implying that near-edge defect levels originated by surface states play an important role in the emission process.[39] Fig. 1f displays the TRPL decay, which was fitted well to a double-exponential function. According to the spectrum, the faster decay time (τ_1 = 2.9 ns) and slower decay time (τ_2 = 25.1 ns) are speculated to be trap-assisted surface recombination and free charge carrier recombination in bulk, respectively. Both decay times are longer than that of $CsPbBr_3$ grown *via* the AVC method (τ_1 = 1.9 ns and τ_2 = 6.8 ns).[40]

3.2. α-Particle-induced pulse shape rise time analysis

The time-of-flight (TOF) technique[41] was adopted to evaluate the charge carrier mobility of the $CsPbBr_3$ single crystal. The schematic diagram of the α-particle (He^{2+})-induced charge carrier transport process in the $CsPbBr_3$ crystal is shown in ESI,† Fig. S2, and the preamplifier pulse signals are analyzed. Under an external electric field, electrons and holes drift toward the anode and cathode immediately. For electron transport mobility calculation, α-particles act on the cathode. Fig. 2a displays the paths and stopping range of α-particles with an energy of 5.5 MeV in the $CsPbBr_3$ single crystals by Monte-Carlo calculations using the SRIM software, and Fig. 2b shows the depth distributions of the α-particles. Due to the shallow penetration depth of the

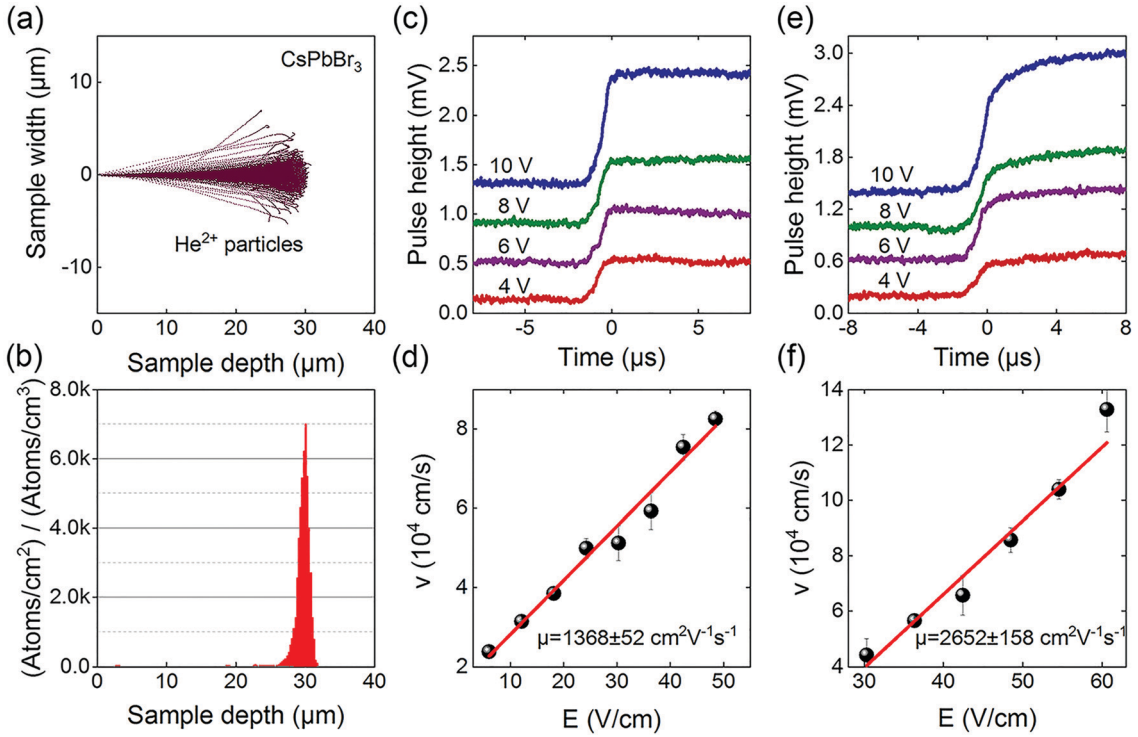

Fig. 2 (a) Stopping and range of α-particles with energy of 5.5 MeV in $CsPbBr_3$ single crystals by Monte-Carlo simulation. (b) Depth distributions of α-particles in $CsPbBr_3$. (c) Time-of-flight transients of electrons using α-particles. (d) Electric field-dependent electron drifting rates from 5 to 50 V cm^{-1}. The resulting electron mobility is 1368 ± 52 cm^2 V^{-1} s^{-1}. (e) Time-of-flight transients of holes using α-particles. (f) Electric field-dependent hole drifting rates from 5 to 50 V cm^{-1}. The resulting hole mobility is 2652 ± 158 cm^2 V^{-1} s^{-1}.

α-particles of about 29 μm obtained from the simulation, the majority of electron–hole pairs were generated and concentrated near the cathode region. Therefore, the resulting charge signal is predominantly attributed to the drift of a single-carrier polarity.[41] The induced transit current signal is converted to pulsed voltage spectra through charge sensitive preamplifier. We collected the induced pulse voltage output from the preamplifier using a high-speed waveform digitizer card. Fig. 2c displays the typical voltage pulse spectrum induced by α-particles at the bias of 4, 6, 8, and 10 V for the electron transport. The 10–90% amplitude rise time of the spectrum was extracted as the carrier drift time, t. The carrier drift velocity can be calculated as $V = d/t$, where d is the thickness of the $CsPbBr_3$ single crystal. Combined with the equation $V = \mu \cdot E$, where μ is the mobility and E is the electric field, by fitting the plot of V–E, as shown in Fig. 2d, the electron mobility was calculated as 1368 ± 52 cm^2 V^{-1} s^{-1}. The charge transport process with holes is similar to electrons when α-particles act on the anode. As results show in Fig. 2e and f, the hole mobility was calculated as 2652 ± 158 cm^2 V^{-1} s^{-1}. The carrier mobility obtained in our work is lower than the reported ~4500 cm^2 V^{-1} s^{-1} for $CsPbBr_3$ nanocrystals,[42] but comparable to that of single crystals (2290 cm^2 V^{-1} s^{-1} for electrons and 2060 cm^2 V^{-1} s^{-1} for holes).[43] The carrier transport property in the as-grown $CsPbBr_3$ single crystals is excellent for high carrier mobility, which guarantees a favorable performance in radiation detection.

3.3. Optimization of device configuration

A sandwich electrode configuration was adopted to fabricate $CsPbBr_3$-based detectors. $CsPbBr_3$ was demonstrated to be a p-type semiconductor in previous reports,[38] and we considered its valence band maximum and the conduction band minimum to be −5.6 and −3.3 eV, respectively. Therefore, Au (ϕ_{Au} = 5.1 eV) is assumed to be a typical high work function electrode metal for $CsPbBr_3$ to inject holes efficiently. Fig. 3a displays a schematic diagram of the Au/$CsPbBr_3$/Au sandwich configuration device and Au-$CsPbBr_3$ contact energy band. φ_1 is the Schottky barrier for hole injection from Au to $CsPbBr_3$ under a positive bias. V_D is the Schottky barrier for hole extraction from $CsPbBr_3$ to Au under a reverse bias. As shown in Fig. 3b, this type of device has a low dark leakage current of 0.4 nA under a 10 V bias, and the resistivity reached 7.85 × 10^9 Ω cm, which is quite a good performance for a radiation detector. However, when a high voltage was applied, the leakage current increased dramatically with 2 μA under 100 V, and the typical I–V curve is presented in Fig. 3b. This issue is a vital challenge that exists in lead halide perovskite materials, which is mainly attributed to vacancy defect activation and ion migration under a high voltage, especially for halogen atoms.[44–47] The charge accumulation and built-in potential caused by ion migration lead to a high leakage current and nonlinearity of the I–V curve.

The photoresponse properties of the Au/$CsPbBr_3$/Au device under different bias and 420 nm LED light with a power of

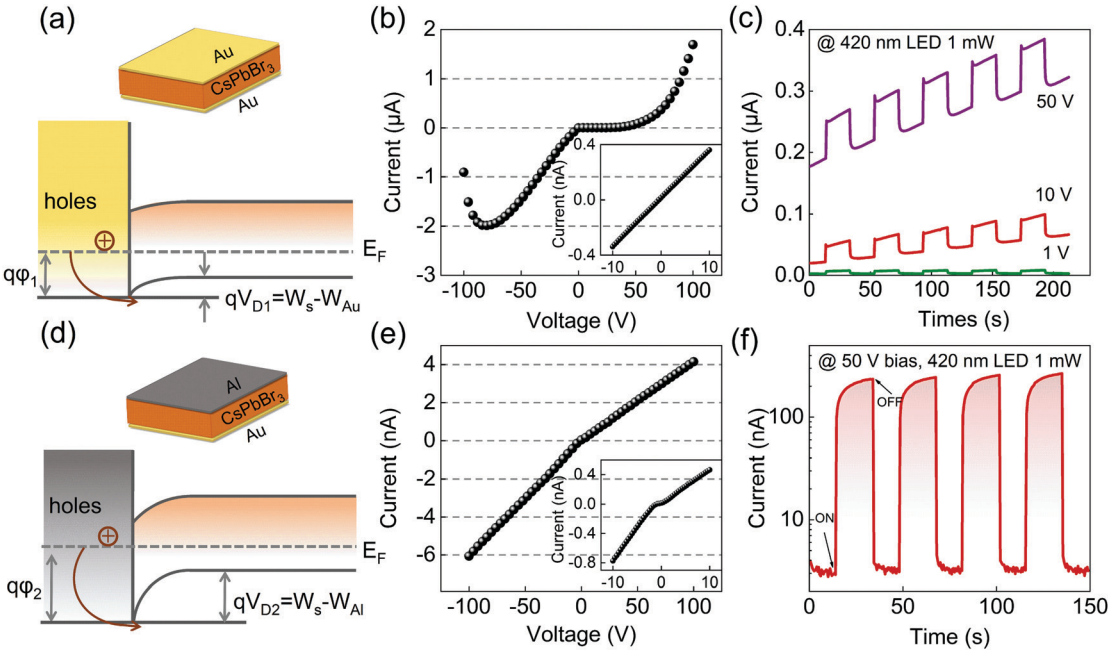

Fig. 3 (a) Au/$CsPbBr_3$/Au device structure and the band diagram of Au-$CsPbBr_3$ contact. (b) Typical *I–V* characteristic curves of the Au/$CsPbBr_3$/Au device at the range of ±10 V and ±100 V. (c) Photoresponse of Au/$CsPbBr_3$/Au device under 1 V, 10 V, 50 V bias, illuminated using a LED with a wavelength of 420 nm and a power of 1 mW. (d) Al/$CsPbBr_3$/Au device structure and the band diagram of Al-$CsPbBr_3$ contact. (e) Typical *I–V* characteristic curves of the Al/$CsPbBr_3$/Au device at the range of ±10 V and ±100 V. (f) Photoresponse of Al/$CsPbBr_3$/Au device under 50 V bias using a LED with a wavelength of 420 nm and a power of 1 mW.

1 mW were further investigated. It is notable that the base line of the dark current drifted continuously with time under a relatively high bias, and the on–off ratio also decreased due to the increase in leakage current, as shown in Fig. 3c. Once the device suffered degradation caused by a high voltage, it was irretrievable under a low bias. This property failure caused by ion migration is a fatal shortcoming for its application in radiation detection since the dark current is expected to be as low as possible to get a high gain factor, and the applied electric field in the device is required to be higher to increase the charge collection efficiency (CCE).

Thus, to suppress ion migration and improve the performance under a high bias, as displayed in Fig. 3d, asymmetric electrodes were designed on the $CsPbBr_3$ device by employing a lower work function metal, Al (ϕ_{Al} = 4.28 eV). Under the working conditions, the electrons were injected from the cathode to $CsPbBr_3$, and holes injected from the anode to $CsPbBr_3$. Because $CsPbBr_3$ is a p-type semiconductor, the lower work function of Al led to greater bending of the energy band of $CsPbBr_3$, thus causing a higher Schottky barrier, ϕ_2, under a positive bias for hole injection from Al to $CsPbBr_3$. The increase in the barrier is beneficial to suppress ion migration in the device under a high voltage. Fig. 3e shows the *I–V* curves of the Al/$CsPbBr_3$/Au device under a low and high bias, where both of them show good linearity with shape asymmetry. The dark current of the new device under a low bias is the same order of magnitude as that of the Au/$CsPbBr_3$/Au device, and surprisingly, under a high voltage, the device also performed well with 4 nA at 100 V. This asymmetric electrode configuration suppresses ion migration significantly without increasing the contact resistance greatly, which ensures the device works under a high bias. Fig. 3f shows the photoresponse property of the Al/$CsPbBr_3$/Au device under 50 V bias and 420 nm LED with 1 mW illumination. Compared with the former device, the base line of the dark current was steady with time, and the on–off ratio reached 10^2, demonstrating a good photoresponse property. Further, the operation stability of the Al/$CsPbBr_3$/Au device was demonstrated to be better than that of the Au/$CsPbBr_3$/Au device. The dark current under a constant 100 V bias was steady within 150 s, which is greatly improved compared with that of the Au/$CsPbBr_3$/Au device, whose dark current increased dramatically within 20 s, as shown in the ESI,† Fig. S3. Therefore, long-time stability under a high voltage was achieved in the optimized device.

3.4. X-ray detection performances of $CsPbBr_3$ detectors

To investigate the X-ray detector performance of the typical Au/$CsPbBr_3$/Au device and the improved asymmetric electrodes Al/$CsPbBr_3$/Au device, their X-ray response and sensitivity were measured. During the measurements, the devices were exposed to a tungsten anode X-ray source, with the tube voltage ranging from 50 to 80 kV and tube current from 1 to 600 μA. To obtain correct sensitivity values, the radiation dose rates were carefully calibrated using both an ion chamber dosimeter and thermoluminescence meters. We measured the dose rates of various tube currents under specific tube voltages and distances, *r*, from the device to the X-ray source. By fitting the data, we obtained a directly proportional relationship between dose rate

and tube current when the tube voltage and distance, r, were fixed. The fitting results of the dose rate as a function of tube current under different tube voltages and distances, r, are presented in the ESI,† Fig. S4. Furthermore, there is a good direct ratio relation between dose rate and $1/r^2$ according to the planar irradiation of the source (ESI,† Fig. S5). Therefore, the dose rate at any tube current and r can be calculated using the calibrated results, and dose rate can be altered accurately by means of changing the tube current.

A schematic illustration of the photoelectric process and photoconductive gain during the working state of detectors is shown in Fig. 4a, and a picture of the $CsPbBr_3$ single crystal X-ray detector is shown in Fig. 4d. As shown in the ESI,† Fig. S6, the stopping power of $CsPbBr_3$ is similar to that of CdTe, and stronger than $MAPbBr_3$ and α-Se, due to its relatively high average atomic number. Ignoring the very thin electrodes, the $CsPbBr_3$ SCs used in this work attenuated almost all the X-ray radiation within the energy range of 50–80 eV. Thus, electron–hole pairs were generated within the bulk SC when illuminated by X-rays. Under a bias, the electrons and holes separated and drifted toward the two electrodes to increase photoconductive gain.

Fig. 4b shows the response of the Au/$CsPbBr_3$/Au device (detector I) upon turning the X-ray source on and off at a field of 1 V mm^{-1}, and under continuously changed X-ray flux at 8 V mm^{-1}, which is the maximum bias for detector I. The results demonstrate a sharp rise and fall edge and steady signal current. The detector sensitivity was defined as $S = (I_{ON} - I_{OFF})$/dose rate, which was calculated by fitting the data. As displayed in Fig. 4c, the sensitivity of detector I under different bias was fitted, and the highest sensitivity was 61 μC Gy^{-1} cm^{-2} under 8 V mm^{-1} and 80 kVp X-rays, which is three times higher than that of the commercially used α-Se detectors[48] working at a much higher field of 10 V μm^{-1} (20 μC Gy^{-1} cm^{-2}) for 60 kVp X-ray detection. Due to the higher CCE, the sensitivity increased with an increase in the electric field. For detector I, the sensitivity of different X-ray photoenergies was also investigated under 1 V mm^{-1}, as demonstrated in the ESI,† Fig. S7. It showed that in the same range of dose rate, the detector has higher sensitivities for X-rays with a lower photoenergy, which is caused by the longer hole drift length. By calculating the linear attenuation coefficient using XCOM of NIST,[49] photons of 50 kVp and 80 kVp are adequately attenuated within the 0.2 mm and 0.7 mm $CsPbBr_3$ samples, respectively. Due to the thinner active layer of 50 kVp, the average hole drift length is longer than that of 80 kVp, which contributes higher photocurrents because of the higher hole mobility compared with electrons (ESI,† Fig. S8). For the same photon energy of X-rays, the sensitivity and CCE were lower in the range of high dose rate, which is mainly due to the higher built-in electric field established by the generated charge carrier under high dose rate exposure (ESI,† Fig. S9). The CCE was calculated as CEE = I_R/I_P, where I_R is the induced photocurrent, and I_P is theoretical photocurrent

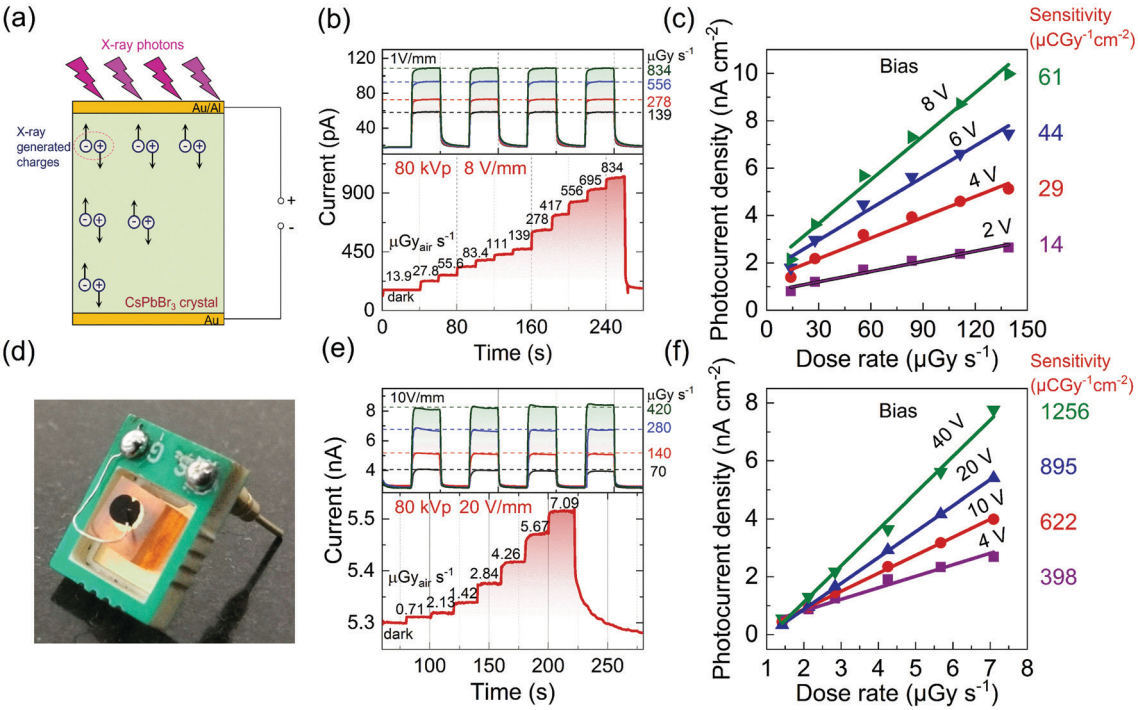

Fig. 4 (a) Schematic illustration of the photoelectric process in the Au(Al)/$CsPbBr_3$/Au devices under X-ray radiation. (b) X-ray photoresponse of the Au/$CsPbBr_3$/Au devices under different dose rates. (c) Dose rate-dependent photocurrent densities of Au/$CsPbBr_3$/Au device under 2 V, 4 V, 6 V and 8 V. The resulting slopes, which represent the X-ray response sensitivities, are 14 C Gy^{-1} cm^{-2}, 29 C Gy^{-1} cm^{-2}, 44 C Gy^{-1} cm^{-2} and 61 C Gy^{-1} cm^{-2}, respectively. (d) $CsPbBr_3$ single crystal X-ray detector. (e) X-ray responses of the Al/$CsPbBr_3$/Au device under variable dose rates, which can bear a higher electric field strength than the Au/$CsPbBr_3$/Au device. (f) X-ray response sensitivities of the Al/$CsPbBr_3$/Au device under 4 V, 10 V, 20 V and 40 V are 398 C Gy^{-1} cm^{-2}, 622 C Gy^{-1} cm^{-2}, 895 C Gy^{-1} cm^{-2} and 1256 C Gy^{-1} cm^{-2}, respectively.

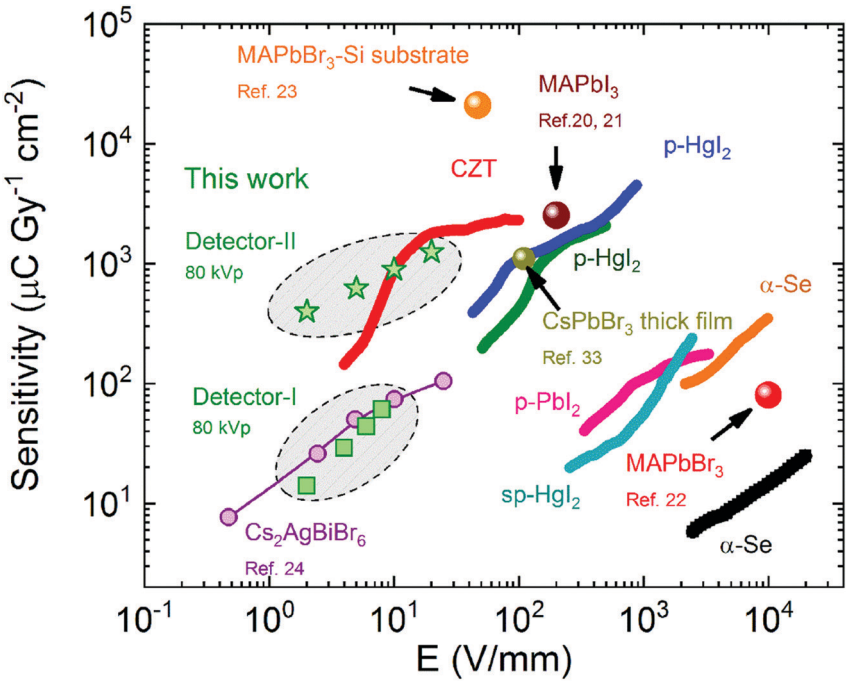

Fig. 5 Comparison of the X-ray detection sensitivities obtain from current state-of-the-art detectors (CdZnTe, α-Se, PbI_2 and HgI_2), recently reported perovskite detectors ($MAPbBr_3$, $MAPbI_3$ and $Cs_2AgBiBr_6$) and the $CsPbBr_3$ detectors in this work. Data for CdZnTe, α-Se, PbI_2 and HgI_2 was extracted from ref. 10.

induced by X-ray ionization, which is defined as[50] $I_P = \varphi\beta e$, where e is the quantity of electric charge. The photon absorption rate φ can be defined as $\varphi = \varepsilon D m_s/E_{ph}$, where ε is the fraction of photons in the sample (100% for the samples in this study), D is the dose rate, m_s is the mass of the sample, and E_{ph} is the photon energy. β is the number of carriers generated by per X-ray photon, which is given by $\beta = E_{ph}/\Delta$, where Δ can be calculated using the empirical model[51] of $\Delta = 1.43 + 2E_g$.

Because of the lower dark current and higher applied bias, the Al/$CsPbBr_3$/Au device (detector II) is expected to have better performance. Fig. 4e shows the X-ray response of detector II upon turning the X-ray source on and off at an electrical field of 10 V mm^{-1}, and under continuously changed X-ray flux at 20 V mm^{-1}. Even under relatively high electric fields, the detector exhibited good on–off ratios, and steady photocurrents. However, the fall edge of the current of detector II is slower than that of detector I with hysteresis of the photocurrent, which may be attributed to the slower recombination of photogenerated electron–hole pairs under a higher electric field strength and the increase in defects in the crystal. Different from detector I, the photocurrent gain was much higher with the same increase in dose rate under a high electric field. The sensitivities of detector II increased significantly with the value of 398 μC Gy^{-1} cm^{-2}, 622 μC Gy^{-1} cm^{-2}, 895 μC Gy^{-1} cm^{-2} and 1256 μC Gy^{-1} cm^{-2} for 4 V, 10 V, 20 V and 40 V, respectively (Fig. 4f). This improvement is mainly attributed to the high CCE of detector II. The ESI,† Fig. S9 shows the CCE values under various electric fields for detector II. Further, we fitted the data using the Hecht equation[41]

$$\mathrm{CCE}(x) = \frac{\mu\tau U}{d^2}\cdot\left(1 - e^{\frac{-d^2}{\mu\tau U}}\right) \quad (1)$$

and the mobility–lifetime product ($\mu\tau$) was calculated as $(2.5 \pm 0.2) \times 10^{-3}$ cm^{-2} V^{-1} under an X-ray dose rate of 7.1 μ Gy^{-1} s^{-1}. A comparison of the sensitivities obtained from published data[10,20–24] is shown in Fig. 5. It reveals that the highest sensitivity obtained in detector II (1256 μC Gy^{-1} cm^{-2}) is 60 times higher than that of the α-Se detector,[48] 15 times higher than that of the Au/$MAPbBr_3$/C_{60}/BCP detector,[22] and 12 times higher than that of the $Cs_2AgBiBr_6$ detector.[24] Thus, $CsPbBr_3$ is a potential material for X-ray detection with high sensitivity and a low working voltage.

4. Conclusion

High quality $CsPbBr_3$ SCs were gown *via* an improved low temperature solution method, which exhibited high transmittance, mobility and carrier mobility–lifetime product. X-ray detectors were fabricated based on our $CsPbBr_3$ SCs. Modification of the device configuration (from Au/$CsPbBr_3$/Au to Al/$CsPbBr_3$/Au) was demonstrated to be an effective method to suppress ion migration under high bias voltages and obtain long-term stability. The optimized detector could work under 50 V with low dark currents of ~3 nA and outstanding photoresponse on–off ratios of $\sim 10^2$. Due to its high CCE at high bias, the sensitivity of the optimized detector reached 1256 μC Gy^{-1} cm^{-2} under 40 V, which exceeds that of most state-of-the-art detectors and recently reported perovskite detectors at the same electric field. Thus, our work demonstrates that $CsPbBr_3$ is an excellent material for sensitive X-ray detection owing to its facile synthesis and excellent detection performance.

Conflicts of interest

There are no conflicts to declare.

Acknowledgements

This work has been financially supported by National Natural Science Foundations of China (U1631116 and 51802262), National Key Research and Development Program of China (2016YFE0115200), the Natural Science Foundation of Shaanxi Province (2019JQ-459), and the Fundamental Research Funds for the Central Universities (3102018jcc036 and 3102019TS0408). At Northwestern University work on hard radiation detector materials was supported by a grant from the Department of Homeland Security ARI program (grant number 2014-DN-077-ARI086-01).

Notes and references

1 A. Sakdinawat and D. Attwood, *Nat. Photonics*, 2010, **4**, 840–848.
2 M. J. Yaffe and J. A. Rowlands, *Phys. Med. Biol.*, 1997, **42**, 1–39.
3 S. O. Kasap, J. B. Frey, G. Belev, O. Tousignant, H. Mani, J. Greenspan, L. Laperriere, O. Bubon, A. Reznik and G. Decrescenzo, *Sensors*, 2011, **11**, 5112–5157.
4 M. J. Yaffe and J. A. Rowlands, *Phys. Med. Biol.*, 1997, **42**, 1–39.
5 S. O. Kasap and J. A. Rowlands, *Proc. IEEE*, 2002, **90**, 591–604.
6 J. P. Moy, *Nucl. Instrum. Methods Phys. Res.*, 2000, **442**, 26–37.
7 S. O. Kasap, *J. Phys. D: Appl. Phys.*, 2000, **33**, 2853–2865.
8 R. A. Street, S. E. Ready, K. V. Schuylenbergh, J. Ho, J. B. Boyce, P. Nylen, K. Shah, L. Melekhov and H. Hermon, *J. Appl. Phys.*, 2002, **91**, 3345–3355.
9 G. Zentai, M. Schieber, L. Partain, R. Pavlyuchkova and C. Proano, *J. Cryst. Growth*, 2005, **275**, 1327–1331.
10 M. Schieber, H. Hermon, A. Zuck, A. I. Vilensky, L. Melekhov, R. Shatunovsky, E. Meerson, Y. Saado, M. Lukach and E. Pinkhasy, *J. Cryst. Growth*, 2001, **225**, 118–123.
11 M. Richter and P. Siffert, *Nucl. Instrum. Methods Phys. Res., Sect. A*, 1992, **322**, 529–537.
12 C. Szeles, *Phys. Status Solidi B*, 2004, **241**, 783–790.
13 S. Shrestha, R. Fischer, G. J. Matt, P. Feldner, T. Michel, A. Osvet, I. Levchuk, B. Merle, S. Golkar, H. Chen, S. F. Tedde, O. Schmidt, R. Hock, M. Rührig, M. Göken, W. Heiss, G. Anton and C. J. Brabec, *Nat. Photonics*, 2017, **11**, 436–440.
14 M. Kulbak, D. Cahen and G. Hodes, *J. Phys. Chem. Lett.*, 2015, **6**, 2452–2456.
15 G. E. Eperon, G. M. Paterno, R. J. Sutton, A. Zampetti, A. A. Haghighirad, F. Cacialli and H. J. Snaith, *J. Mater. Chem. A*, 2015, **3**, 19688–19695.
16 R. J. Sutton, G. E. Eperon, L. Miranda, E. S. Parrott, B. A. Kamino, J. B. Patel, M. T. Hörantner, M. B. Johnston, A. A. Haghighirad and D. T. Moore, *Adv. Energy Mater.*, 2016, **6**, 1–6.
17 Z.-K. Tan, R. S. Moghaddam, M. L. Lai, P. Docampo, R. Higler, F. Deschler, M. Price, A. Sadhanala, L. M. Pazos and D. Credgington, *Nat. Nanotechnol.*, 2014, **9**, 687–692.
18 H. Zhu, Y. Fu, F. Meng, X. Wu, Z. Gong, Q. Ding, M. V. Gustafsson, M. T. Trinh, S. Jin and X. Zhu, *Nat. Mater.*, 2015, **14**, 636.
19 D. Clark, C. Stoumpos, F. Saouma, M. Kanatzidis and J. Jang, *Phys. Rev. B*, 2016, **93**, 195202.
20 S. Yakunin, M. Sytnyk, D. Kriegner, S. Shrestha, M. Richter, G. J. Matt, H. Azimi, C. J. Brabec, J. Stangl and M. V. Kovalenko, *Nat. Photonics*, 2015, **9**, 444–449.
21 S. Shrestha, R. Fischer, G. J. Matt, P. Feldner, T. Michel, A. Osvet, I. Levchuk, B. Merle, S. Golkar and H. Chen, *Nat. Photonics*, 2017, **11**, 436–440.
22 H. Wei, Y. Fang, P. Mulligan, W. Chuirazzi, H. Fang, C. Wang, B. R. Ecker, Y. Gao, M. A. Loi and L. Cao, *Nat. Photonics*, 2016, **10**, 333–339.
23 W. Wei, Y. Zhang, Q. Xu, H. Wei, Y. Fang, Q. Wang, Y. Deng, T. Li, A. Gruverman and L. Cao, *Nat. Photonics*, 2017, **11**, 315–321.
24 W. Pan, H. Wu, J. Luo, Z. Deng, C. Ge, C. Chen, X. Jiang, W. J. Yin, G. Niu and L. Zhu, *Nat. Photonics*, 2017, **11**, 726.
25 L. Li, X. Liu, H. Zhang, B. Zhang, W. Jie, P. J. Sellin, C. Hu, G. Zeng and Y. Xu, *ACS Appl. Mater. Interfaces*, 2019, **11**, 7522–7528.
26 Y. He, L. Matei, H. J. Jung, K. M. McCall, M. Chen, C. C. Stoumpos, Z. Liu, J. A. Peters, D. Y. Chung, B. W. Wessels, M. R. Wasielewski, V. P. Dravid, A. Burger and M. G. Kanatzidis, *Nat. Commun.*, 2018, **9**, 1609.
27 Q. Xu, W. Shao, Y. Li, X. Zhang, X. Ouyang, J. Liu, B. Liu, Z. Wu, X. Ouyang, X. Tang and W. Jia, *ACS Appl. Mater. Interfaces*, 2019, **11**, 9679–9684.
28 C. C. Stoumpos, C. D. Malliakas, J. A. Peters, Z. Liu, M. Sebastian, J. Im, T. C. Chasapis, A. C. Wibowo, D. Y. Chung and A. J. Freeman, *Cryst. Growth Des.*, 2013, **13**, 2722–2727.
29 J. Song, Q. Cui, J. Li, J. Xu, Y. Wang, L. Xu, J. Xue, Y. Dong, T. Tian and H. Sun, *Adv. Opt. Mater.*, 2017, **5**, 1700157.
30 M. I. Saidaminov, A. Haque, J. M. Almutlaq, S. P. Sarmah, X. Miao, R. Begum, A. A. Zhumekenov, I. Dursun, N. Cho and B. Murali, *Adv. Opt. Mater.*, 2017, **5**, 1600704.
31 D. N. Dirin, I. Cherniukh, S. Yakunin, Y. Shynkarenko and M. V. Kovalenko, *Chem. Mater.*, 2016, **28**, 8470–8474.
32 J. Ding, S. Du, Z. Zuo, Y. Zhao, H. Cui and X. Zhan, *J. Phys. Chem. C*, 2017, **121**, 4917–4923.
33 Z. Gou, S. Huanglong, W. Ke, H. Sun, H. Tian, X. Gao, X. Zhu, D. Yang and P. Wangyang, *Phys. Status Solidi RRL*, 2019, **13**, 1900094.
34 W. Pan, B. Yang, G. Niu, K. H. Xue, X. Du, L. Yin, M. Zhang, H. Wu, X. S. Miao and J. Tang, *Adv. Mater.*, 2019, **31**, 1904405.
35 X. Ren, Z. Yang, D. Yang, X. Zhang, D. Cui, Y. Liu, Q. Wei, H. Fan and S. F. Liu, *Nanoscale*, 2016, **8**, 3816–3822.
36 G. E. Eperon and D. S. Ginger, *Nat. Energy*, 2016, **1**, 16109.

37 H. Zhang, X. Liu, J. Dong, H. Yu, C. Zhou, B. Zhang, Y. Xu and W. Jie, *Cryst. Growth Des.*, 2017, **17**, 6426–6431.
38 Y. He, L. Matei, H. J. Jung, K. M. Mccall, M. Chen, C. C. Stoumpos, Z. Liu, J. A. Peters, D. Y. Chung and B. W. Wessels, *Nat. Commun.*, 2018, **9**, 1609.
39 D. J. As, F. Schmilgus, C. Wang, B. Schottker, D. Schikora and K. Lischka, *Appl. Phys. Lett.*, 1997, **70**, 1311–1313.
40 J. Ding, S. Du, Z. Zuo, Y. Zhao, H. Cui and X. Zhan, *J. Phys. Chem. C*, 2017, **121**, 4917–4923.
41 P. J. Sellin, A. W. Davies, S. Gkoumas, A. Lohstroh, M. E. Ozsan, J. Parkin, V. Perumal, G. Prekas and M. C. Veale, *Nucl. Instrum. Methods Phys. Res., Sect. B*, 2008, **266**, 1300–1306.
42 G. R. Yettapu, D. Talukdar, S. Sarkar, A. Swarnkar, A. Nag, P. Ghosh and P. Mandal, *Nano Lett.*, 2016, **16**, 4838–4848.
43 J. Song, Q. Cui, J. Li, J. Xu, Y. Wang, L. Xu, J. Xue, Y. Dong, T. Tian and H. Sun, *Adv. Opt. Mater.*, 2017, **5**, 1700157.
44 T. Shi, W. Yin, F. Hong, K. Zhu and Y. Yan, *Appl. Phys. Lett.*, 2015, **106**, 103902.
45 C. Eames, J. M. Frost, P. R. F. Barnes, B. C. Oregan, A. Walsh and M. S. Islam, *Nat. Commun.*, 2015, **6**, 7497.
46 W. Ming, S. Chen and M. Du, *J. Mater. Chem.*, 2016, **4**, 16975–16981.
47 J. Kang and L. Wang, *J. Phys. Chem. Lett.*, 2017, **8**, 489–493.
48 W. Zhao and J. A. Rowlands, *Med. Phys.*, 1995, **22**, 1595–1604.
49 M. Berger, *XCOM photon cross section database*, NIST physics laboratory, Gaithersburg, MA, 1998.
50 B. Fraboni, A. Ciavatti, F. Merlo, L. Pasquini, A. Cavallini, A. Quaranta, A. Bonfiglio and A. Fraleonimorgera, *Adv. Mater.*, 2012, **24**, 2289–2293.
51 R. Devanathan, L. R. Corrales, F. Gao and W. J. Weber, *Nucl. Instrum. Methods Phys. Res., Sect. A*, 2006, **565**, 637–649.